Available online at www.sciencedirect.com
SCIENCE DIRECT®
Earth and Planetary Science Letters xx (2004) xxx–xxx
EPSL
www.elsevier.com/locate/epsl

Yield strength and strain hardening of MgO up to 8 GPa measured in the deformation-DIA with monochromatic X-ray diffraction

Takeyuki Uchida*, Yanbin Wang[1], Mark L. Rivers[2], Steve R. Sutton[3]

Consortium for Advanced Radiation Sources, The University of Chicago, 5640 South Ellis Avenue, Chicago, Illinois, 60637, USA

Received 1 April 2004; received in revised form 12 July 2004; accepted 16 July 2004
Editor: S. King

Abstract

Cylindrical polycrystalline MgO samples have been deformed with total axial strains up to 35% at pressures up to 8 GPa. Hysteresis loops between elastic lattice strain and total axial strain were established by repeatedly shortening and lengthening the samples at selected strain rates. The yield point was identified as the first deviation from linearity in the lattice strain versus total strain curves. MgO samples yielded at low total strains (<1%) and the yield strength (ca. 0.5 GPa) was insensitive to pressure. Beyond the yield point, MgO showed a strong strain-hardening behavior, characterized by an initial rapid increase in flow stress, followed by a linear stage with a constant hardening parameter. At pressures below 5 GPa, lattice strains associated with reflections 200, 220, and 222 diverged with increasing total strain. Above 5 GPa, these lattice strains converged, suggesting a possible change in flow mechanism.

Keywords: deformation; initial yield strength; flow stress; strain hardening; lattice strain

1. Introduction

Because of the needs in understanding rheological properties of the Earth's interior, the yield strength of MgO at high pressure has been studied extensively in the past decade using a variety of experimental techniques, including measurements of radial pressure distribution and final sample thickness in the diamond anvil cell (DAC) [1,2], peak width of powder X-ray diffraction patterns in a conventional DIA [3], and distortion of the diffraction Debye rings recorded perpendicular to the loading axis in the DAC ([4] and the review therein). In all these studies, differential stress was not an independently controllable parameter, but rather a consequence of either pressure gradients or elasticity mismatch at grain contacts.

* Corresponding author. Tel.: +1 630 252 0432; fax: +1 630 252 0436.
E-mail addresses: uchida@cars.uchicago.edu (T. Uchida), wang@cars.uchicago.edu (Y. Wang), rivers@cars.uchicago.edu (M.L. Rivers), sutton@cars.uchicago.edu (S.R. Sutton).
[1] Tel.: +1 630 252 0425; fax: +1 630 252 0436.
[2] Tel.: +1 630 252 0422; fax: +1 630 252 0436.
[3] Tel.: +1 630 252 0426; fax: +1 630 252 0436.

0012-821X/$ - see front matter © 2004 Published by Elsevier B.V.
doi:10.1016/j.epsl.2004.07.023

Due to this inability to control differential stress, it has not been possible to determine whether the sample is within the elastic or plastic regime. As a result, previous estimates on the "yield strength" varied by more than a factor of 10.

In this report, we present results obtained by triaxial deformation experiments on cylindrical polycrystalline MgO samples using the deformation-DIA (D-DIA) [5]. We demonstrate that (1) by advancing (retracting) the differential rams in the D-DIA, samples can be shortened (lengthened) as the differential stress levels are increased (decreased) at a given pressure, allowing controlled experiments within either the elastic or the plastic regime, (2) lattice strains determined from distortion of the diffraction Debye rings can be used as a stress gauge, as has been demonstrated in previous radial diffraction experiments ([4] and references therein), (3) the initial yield point can be detected as the deviation from linearity in a plot of lattice strain versus total axial strain, and (4) the strength of MgO increases with total strain, with significant work hardening. The hardening can be quantified by a hardening parameter based on in situ measurements up to 35% total axial strain and possible change in flow mechanism may also be detected from the different strain-hardening behavior observed for various reflections.

2. Experiment

2.1. Monochromatic X-ray diffraction methods

Details of the D-DIA apparatus have been described elsewhere [5]. The D-DIA module is compressed in the 250-ton press [6] installed at the GSECARS 13-BM-D synchrotron radiation beamline [7] at the Advanced Photon Source (APS). An incident X-ray beam was monochromatized at an energy of 65.0 keV (0.191 Å wavelength) by a Si (111) monochromator. Two pairs of tungsten carbide slits were placed in the beam path for diffraction to aperture the incident X-rays to 100×100 μm. The two-dimensional (2-D) diffraction patterns were collected by a Bruker SMART 1500 X-ray charge-coupled device (CCD) detector (1024×1024 pixels). By driving the slits out of the beam path, radiographic image of the cell assembly was taken to measure the sample length during deformation cycles with a 3×3 mm monochromatic X-ray beam. The X-ray imaging system, adopted from the X-ray tomography setup at GSECARS [8], was mounted on the press frame (e.g., [9]). The PentaMax CCD camera (1300×1000 pixels) collected the visible-light image on a YAG scintillator produced by the X-ray absorption contrast of the cell assembly with 1.3 μm/pixel resolution.

The pressure medium (6 mm edge length cube) was a mixture of amorphous boron and epoxy resin, with a sample chamber of 1.6 mm diameter stacked with the following materials (from top to bottom): crushable Al_2O_3 cylinder, sintered Al_2O_3 piston, packed MgO powder (1.5 mm initial height and 1.2 mm diameter, <10 μm grain size) surrounded by a hexagonal BN sleeve, sintered Al_2O_3 piston and crushable Al_2O_3 cylinder. In the high-temperature cell, the sample column was surrounded by a graphite heater tube (4 mm height) with platinum foils at the top and bottom of the heater for electric contact.

Prior to an experiment, detector orientation relative to the incident X-ray beam was calibrated using the diffraction pattern from a standard (CeO_2). The sample assembly was then loaded in the D-DIA and the sample–detector distance was determined from the diffraction pattern of MgO at ambient conditions. Under pressure, the differential rams were advanced (retracted) at constant speeds to shorten (lengthen) the sample, while diffraction patterns and radiographic images were repeatedly recorded with 300 and 100 s of exposure times, respectively, at the vertical center of the sample.

We report results from two experiments (D0466 and D0471). In run D0466, the sample was exposed to four compression–extension cycles at each of four pressures (0.5, 1.0, 2.0 GPa and back to 0.5 GPa). In run D0471, pressure was first increased to 4.9 GPa and then the sample was shortened and lengthened under an average pressure of about 6.4 GPa (4.9–7.9 GPa). After the deformation cycle, the sample temperature was increased, but in the present paper, we will focus on room temperature deformation results only.

2.2. Data analysis

Theory describing elastic lattice strain under uniaxial compression has been developed for various

crystallographic systems (cubic by [10], hexagonal by [11], and all others by [12]) and the results have been applied to radial diffraction experiments in the DAC (e.g., [4,13]). Our data reduction technique is similar to that of [4]. After spatial and flat field corrections, each 2-D diffraction pattern (Fig. 1(a)), which is plotted in polar coordinates of reciprocal d-spacing versus detector azimuth χ, is converted into Cartesian coordinates (A "cake" form; Fig. 1(b)) using the software package FIT2D [14]. In our case, χ=0 is arbitrarily defined in the horizontal direction, parallel to the minimum principal stress axis. The diffraction data in Cartesian coordinates are then converted into a series of 1-D (intensity versus 2θ) diffraction patterns, by binning the data in 1° intervals of the detector χ angle. Each of the 1-D patterns is fit by an automated curve-fitting program to obtain 2θ values for the peaks, so that the peak positions (in d-spacing) are determined as a function of true azimuth angle φ, which is modified based on the dependence of the detector azimuth χ on the 2θ angle: $\sin\varphi=\cos\theta\sin\chi$ (see [4] or [15] for details).

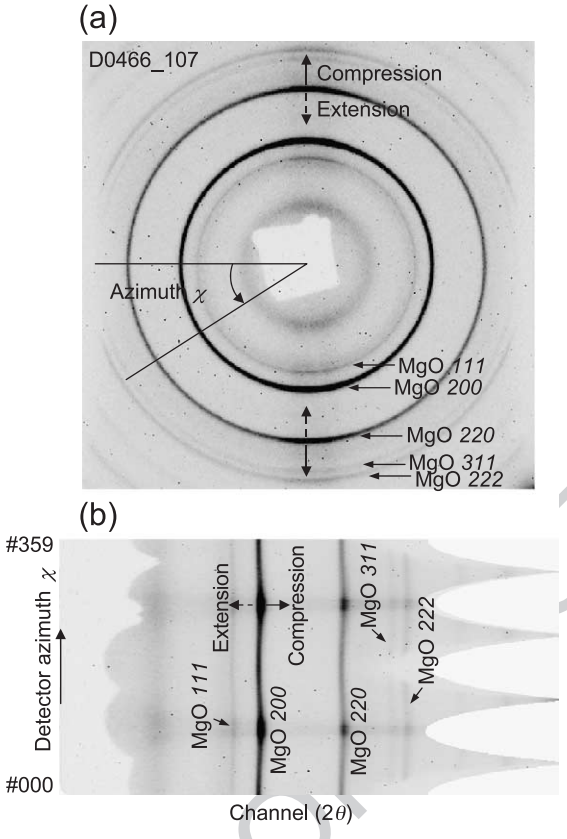

Fig. 1. (a) An example of diffraction Debye ring recorded parallel to compression axis, collected in the second-stage hardening. Solid and dashed arrow indicates the direction of Debye ring distortion. When the sample is shortened (lengthened), Debye ring distorts in the direction of solid (dashed) arrow. (b) A "cake" form, converted from polar coordinates of reciprocal d-spacing versus detector azimuth χ using the software package FIT2D by binning data at 1° steps. The vertical axis is detector azimuth angles, from 0° to 359° (from bottom to top), of the Debye rings, with zero degree arbitrarily defined as diffraction vector being horizontal (parallel to the minimum principal stress axis), and the horizontal axis is 2θ, from 0° to 10° (left to right). Intensity variation is caused by absorption of cubic-BN anvils. In the vertical direction (azimuth χ~90° and 270°), X-ray does not go through cubic-BN anvil and therefore intensity is stronger.

As in conventional deformation experiments, we denote the uniaxial stress field at the center of the sample as (modified from [10]),

$$\sigma_{ij} = \begin{pmatrix} \sigma_1 & 0 & 0 \\ 0 & \sigma_3 & 0 \\ 0 & 0 & \sigma_3 \end{pmatrix} = \begin{pmatrix} \sigma_p & 0 & 0 \\ 0 & \sigma_p & 0 \\ 0 & 0 & \sigma_p \end{pmatrix} + \begin{pmatrix} 2t/3 & 0 & 0 \\ 0 & -t/3 & 0 \\ 0 & 0 & -t/3 \end{pmatrix}, \quad (1)$$

where σ_1 and σ_3 represent the maximum and minimum principal stresses, respectively, with compression being positive. Hydrostatic and differential stresses are defined as $\sigma_p(=(\sigma_1+2\sigma_3)/3)$ and $t(=\sigma_1-\sigma_3)$, respectively. The lattice strain $\varepsilon(\varphi,hkl)$ of any d-spacing with Miller index (hkl) in a polycrystalline sample with random grain orientation is expressed as

$$\varepsilon(\phi, hkl) = \varepsilon_p - \varepsilon_t(hkl)\left(1 - 3\sin^2\phi\right), \quad (2)$$

where ε_p is hydrostatic strain and $\varepsilon_t(hkl)$ the "differential lattice strain" due to the differential stress. The magnitude of $\varepsilon_t(hkl)$ is obtained by fitting each reflection distortion in the cake form (Fig. 2). We assume a simple elastic relation:

$$t(hkl) = 6G(hkl)\varepsilon_t(hkl), \quad (3)$$

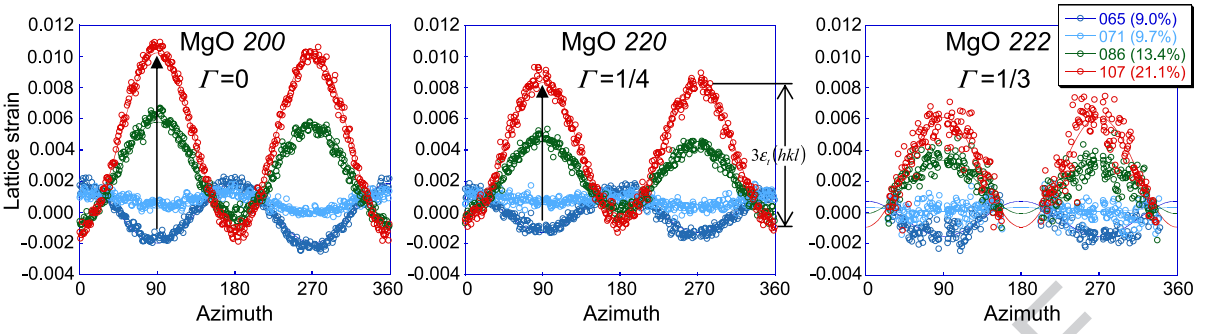

Fig. 2. An example of the azimuthal distortion of lattice strain $\varepsilon_t(hkl)$ for 200, 220 and 222 taken from the deformation cycle at 1.0 GPa. The legend shows the data file number with total axial strain in brackets. Data 065 were collected at the onset of deformation, 071 at the yield point, 086 in the first-stage hardening, and 107 in the second-stage hardening. Because the deformation cycle at 0.5 GPa was completed with extension, the lattice strain was negative to begin with (65). Depending on $\Gamma(hkl)(=(h^2k^2+k^2l^2+l^2h^2)/(h^2+k^2+l^2)^2)$, magnitude of lattice strains are systematically different. Note the change in the direction of lattice strain modulation (indicated by arrow in 200 and 220), due to reversing differential ram directions (positive: compression; negative: extension).

where $G(hkl)$ is the shear modulus. For MgO, the $t(hkl)$'s are expressed as

$$t(222) = 3\varepsilon_t(222)/[S_{44}/2], \tag{4}$$

$$t(200) = 3\varepsilon_t(200)/[S_{11} - S_{12}], \tag{5}$$

and

$$t(220) = 3\varepsilon_t(220)/[1/4(S_{11} - S_{12}) + 3/8S_{44}]. \tag{6}$$

Note that here we do not assume either iso-stress or iso-strain models and differential stresses $t(hkl)$ are not necessarily identical. We consider certain diffraction plane (hkl) and assume stress=elastic constant× strain on the plane of interest.

Beyond the yield point, the sample starts plastic deformation and stress distribution becomes heterogeneous. It is not so obvious whether the elastic constants in Eqs. (4)–(6) are still applicable in the plastic regime. However, lattice strain observed in diffraction Debye ring is elastic and it essentially returns to zero when both pressure and stress are released. In this report, we use the elastic lattice strain to compute differential stress using Eqs. (4)–(6), even after the sample yields, and then discuss feasibility of lattice strain as stress gauge rather than justify the applicability of the elastic constants in Eqs. (4)–(6) in plastic regime.

Hydrostatic stress (pressure) is obtained from the hydrostatic strain ε_p,

$$\sigma_p = K_T \times 3\varepsilon_p = (1/S_{11} + 2S_{12})\varepsilon_p, \tag{7}$$

where K_T is isothermal bulk modulus. At high pressures, the hydrostatic strain is finite and therefore Eq. (7) needs to be extended according to the third-order Birch–Murnaghan equation of state (EOS)

$$\sigma_p = \left(\frac{3}{2}\right)K_T\left((1-\varepsilon_p)^{-7} - (1-\varepsilon_p)^{-5}\right) \times \left[1 - \left(\frac{3}{4}\right)(4 - K_T')\left((1-\varepsilon_p)^{-2} - 1\right)\right], \tag{8}$$

where K_T' is the pressure derivative of K_T. In the present study, both K_T and S_{ij} are taken from [17].

The total axial strain of the sample is defined as

$$\varepsilon_{\text{total}} = (l_0 - l)/l_0, \tag{9}$$

where l_0 and l are the sample lengths measured from radiographic images in the vertical direction (parallel to both the cylindrical axis of the sample and σ_1) at a reference point and under a given differential stress during deformation cycles, respectively. The reference point is arbitrarily chosen at the very first point of the first deformation cycle. Note that while X-ray lattice strains are elastic and are a manifestation of volumetric (pressure) and differential stresses, the total axial strain contains significant plastic component. This will be denoted as "total strain" to be distinguishable from the lattice strains.

3. Results

Fig. 3 plots differential lattice strains $\varepsilon_t(hkl)$ against total axial strain ε_{total}. As can be seen in the azimuth dependence of lattice strain shown in Fig. 2, peak position of each diffraction line is fit by Eq. (2). The error bar in Fig. 3, representing one standard deviation in the least-squares fit, indicates the magnitude of scattering in Fig. 2 and indirectly the error in curve-fitting result of peak position. Intensity of 111 reflection is fairly weak compared to 200 and 220 reflections, resulting in large scatter of lattice strain (peak position) in azimuth dependence (Fig. 2). Thus, the error bar of 111 reflection is larger than that of other two reflections in Fig. 3. Intrinsic lattice strain change is more significant than the size of the errors for all reflections.

The hysteresis loop identifies the total strain threshold for the elastic regime, i.e., the initial linear segment after the differential rams are reversed. Note that after the first compression–extension cycle, the lattice strains for different subsets of grains contributing various *hkl* reflections do not return to zero at the same total strain level, due to the build up of residual strain after plastic deformation.

The initial yield point is identified as the deviation from the linear lattice strain versus total strain relation in Fig. 3. The yield point is more clearly and accurately detected by examining the derivatives of the curve. Fig. 4 shows details of the lattice strain change during the second deformation cycle (for 200, 220, and 222 reflections), as well as the derivative of the lattice strain versus total strain curve (only for 220 reflection). In an ideal elasto-plastic material, the derivative curve should start out as a flat line (constant slope corresponding to elastic constants for the given crystallographic direction), then become zero beyond the yield point (ideal plasticity, with no strain hardening). The elastic flat line in the derivative is observed in our data (Fig.

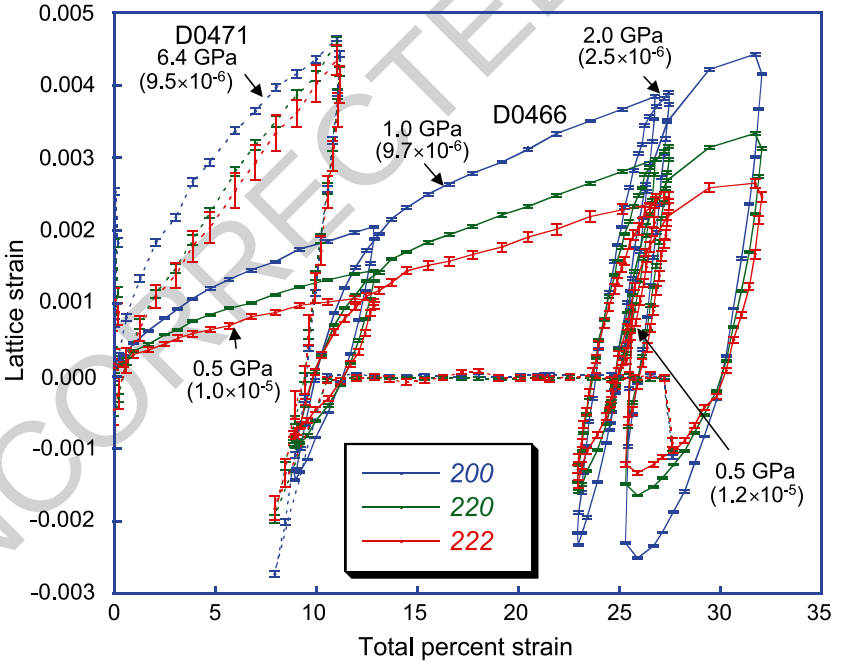

Fig. 3. Lattice strain (elastic) versus total axial percent strain. The reference sample length was arbitrarily chosen at the very beginning of the first deformation cycle. For each lattice strain, the linear relationship between lattice strain and total strain is limited to very small total strains (<1%). Above the linear (elastic) regime, the slope changes with increasing total strain, indicating significant work hardening. Note that the difference in lattice strain between 200 and 222 increases with total strain at low pressures (up to 2 GPa), whereas the difference diminishes with increasing total strain at 6.4 GPa. Pressure is labeled with the sample strain rates (in s^{-1}) for sample shortening in brackets.

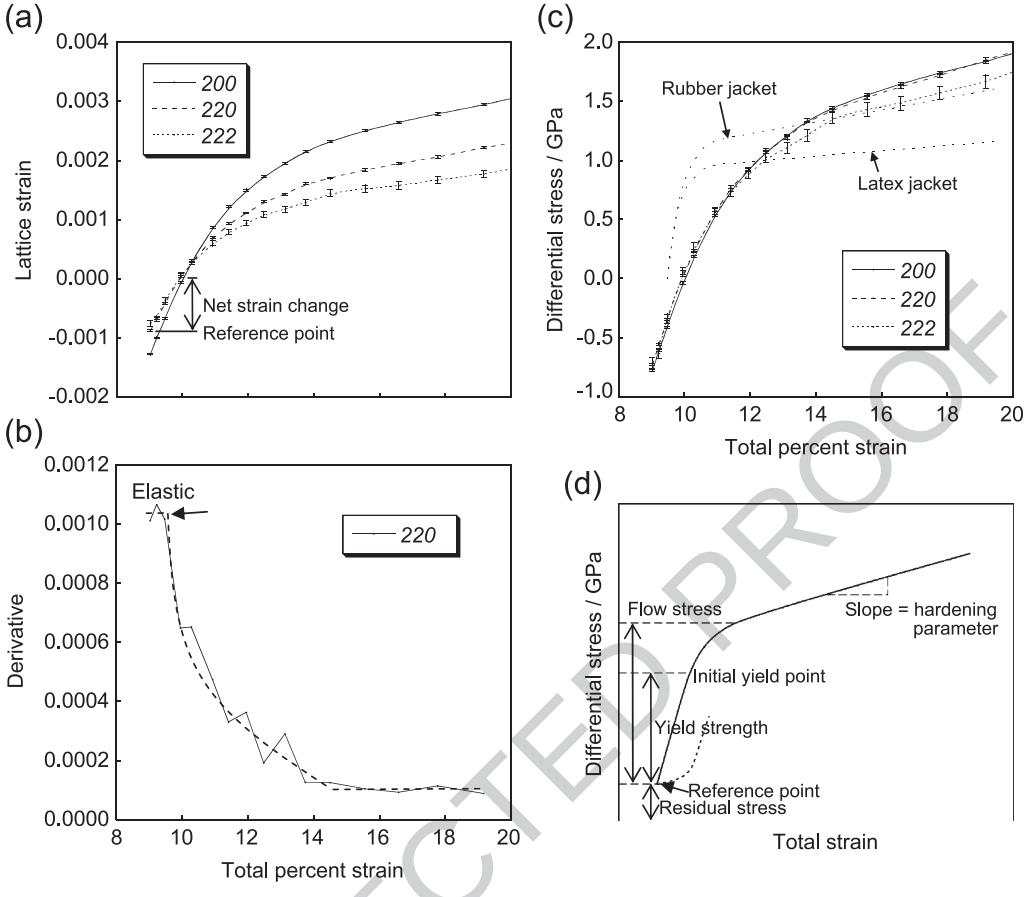

Fig. 4. An example of (a) detail lattice strain change during the deformation cycle at 1.0 GPa, and (b) derivative of lattice strain versus total strain curve in 220 reflection, taken from the deformation cycle at 1.0 GPa. Yield point is defined as the initial deviation from linearity in (a) or abrupt change (indicated by arrow) from elastic to elasto-plastic regimes in the derivative in (b). The sample reaches steady-state at around 14% total strain, where lattice strain linearly increases with total strain. The dashed curves are guide to the eye. (c) Differential stress computed from Eqs. (4)–(6). For comparison, stress data of Paterson and Weaver [14] are plotted by normalizing the horizontal scale with jacketing material (rubber or latex) indicated. (d) Schematic illustration of stress–strain relation. Initial yield point is identified as the first deviation from linearity. Yield strength is the differential stress at initial yield point. Flow stress is differential stress after the sample yields and therefore flow stress>yield strength. Because of multiple deformation cycle, lattice strain contains residual strain at the reference point. To normalize the stress level, yield strength is computed from net strain change shown in (a).

4(b)), followed by an abrupt change in slope (indicated by arrow in Fig. 4(b)), corresponding to the initial yield point. Beyond the initial yield point, however, the derivative first decreases rapidly and then becomes a non-zero constant (Fig. 4(b)), while the lattice strain increases linearly (Fig. 4(a)). This is the direct observation of strain hardening in MgO under high pressure. To distinguish differential stresses at different stages during deformation, we will refer to the differential stress of the initial yield point as “initial yield strength”, and the differential stress beyond the initial yield point as “flow stress” as shown in Fig. 4(d).

When the direction of differential rams is reversed, the observed lattice strain is in elastic regime with significant residual strain (reference point in Fig. 4(d)). To measure the initial yield strength, we first normalize the strain level, determining the net lattice strain change of the linear segment between the first point of each compression cycle and the yield point, as indicated by the arrow in Fig. 4(a). The same process is also

t1.1 Table 1
t1.2 Initial yield strength

Deformation	Cycle	Pressure (GPa)	Strength 200 (GPa)	Strength 220 (GPa)	Strength 222 (GPa)
Compression	D0466 2	0.36	0.29(1)	0.29(1)	0.32(2)
	D0466 3	0.91	0.58(1)	0.60(1)	0.63(3)
	D0466 4	0.13	0.76(1)	0.79(1)	0.80(2)
	D0477	5.08	0.50(2)	0.54(3)	0.54(8)
Average			0.53	0.56	0.57
Extension	D0466 2	0.79	0.57(1)	0.61(1)	0.65(3)
	D0466 3	1.21	0.79(1)	0.84(1)	0.80(3)
	D0466 4	0.32	0.39(1)	0.43(1)	0.50(2)
	D0477	7.16	0.80(1)	0.84(3)	0.87(11)
Average			0.64	0.68	0.71

t1.15 Numbers in parenthesis indicate standard deviation.

applied to the linear segment for each extension cycle. There is no systematic difference in the net strain change for both compression and extension cycles, because extensive yield is achieved by compression by surrounding material in radial direction ($\sigma_3>\sigma_1$), which is one of the critical differences between high pressure deformation experiment and conventional extension test ($\sigma_3=0$). In our measurement, the net total strain change includes both extensive and compressive components, and the extensive strength should be equal to compressive strength under pressure. Thus, the net total strain change is divided by 2 and the initial yield strength is computed from the half of net lattice strain change using Eqs. (4)–(6). The yield strength thus calculated is summarized in Table 1 and plotted in Fig. 5, together with previous differential stress data for comparison.

Both samples, even after exposed to 35% total strain, showed no systematic X-ray intensity variation, exhibiting no direct evidence for texture development. Intensity variation observed in Fig. 1 is due to the absorption of the cubic-BN anvils, which may have overshadowed the intensity variations caused by preferred orientation. An intensity correction scheme is under development to analyze the effect of preferred orientation.

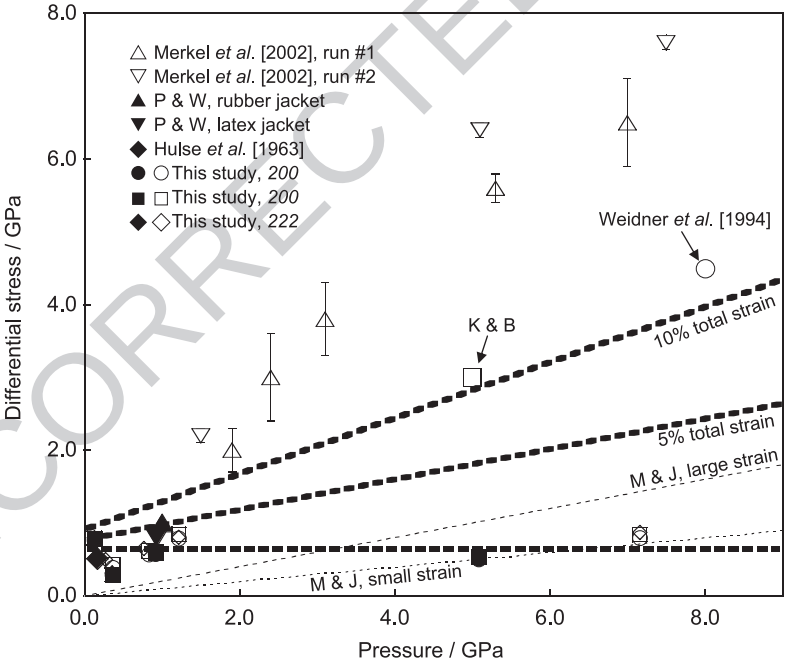

Fig. 5. Comparison of differential stress data. Only the initial yield points from our data are shown, as the flow stress varies greatly with total axial strain. Solid and open symbols in our data indicate the data collected during compression and extension cycles, respectively. Heavy dashed horizontal line is a fit to our yield stress data. Any differential stress above this dashed line should be called "flow stress" rather than "yield strength" [1–3]. Two other heavy dashed lines indicate differential stress level at 5% and 10% total strains. K&B: Kinsland and Bassett [1]; M&J: Meade and Jeanloz [2]; P&W: Paterson and Weaver [14].

4. Discussion

Our yield stress data are rather insensitive to pressure and, within the resolution, can be regarded as a constant at pressures from 0.5 to 7 GPa (Table 1)). On the other hand, all previous differential stress measurements in the DAC and multianvil apparatus, which could not quantify the total sample strain, yielded values much higher (Fig. 5). Our results indicate that these previous high pressure deformation data do not reflect initial yield strength, but rather certain flow stress at some unknown total strain, although some of those studies claimed that they measured "yield strength" [1–3]. This explains the wide scatter in those measurements: Flow stress of MgO depends strongly on total strain, due to strain hardening (Fig. 3). From our results, we can estimate total strain level (dashed line in Fig. 5) in the previous studies. Over 10% total strain should have achieved.

Our results show that strain hardening of MgO is characterized by two different stages (Fig. 4). In the first stage, from immediately after the initial yield point to about 5% total strain, the flow stress rapidly increases with total strain. The second stage, where lattice strain linearly increases with increasing total strain, may be quantitatively characterized by a hardening parameter $(\partial\varepsilon_t(hkl)/\partial\varepsilon_{\text{total}})(\text{or}(\partial t/\partial\varepsilon_{\text{total}})$ if lattice strain can be converted to stress). The hardening parameter is insensitive to pressure below 2 GPa (Fig. 3, D0466). Even after the sample went through compression and extension cycles at several different pressures, lattice strain in the second stage hardening almost linearly increases with increasing total strain, following a unique trend for each *hkl*. In D0471 (higher pressure), hardening parameter is larger than that in D0466 even when arbitrariness in reference point of sample length is taken into account, implying possible change in flow dynamics. This second-stage hardening has similarities with the elastic regime in that differential stress linearly increases with increasing total strain and that the magnitude of lattice strain is greatest for 200 and least for 222. To distinguish these two stages, one must carefully examine the relationship between lattice strain and total strain.

Hulse et al. [18] and Paterson and Weaver [19] deformed cylindrical polycrystalline MgO samples using a gas-medium deformation apparatus. The achievable pressure range was limited to 1 GPa and yet their differential stress data are comparable to our low pressure data at 0.5 and 1.0 GPa (Fig. 5). In addition to the strength data, our data also agree with these conventional deformation results in that the sample reaches initial yield point within 1% of total strain, and that the sample shows strong strain hardening (Figs. 3 and 4(c)). If one converts the net lattice strain change from the 15% to 20% total strain, using the 220 reflection as a stress gauge, the flow stress increases by 0.4 GPa, resulting in a hardening parameter $\partial t/\partial\varepsilon_{\text{total}}$ to be 0.08 GPa per percent strain. For comparison, data of [19] gave a hardening parameter of 0.05 GPa per percent strain. Part of the discrepancy may be attributed to the choice of l_0. If l_0 is chosen at the very beginning of the second deformation cycle, the hardening parameter becomes smaller. The differential stress computed from different reflection may give varying estimates within about 10–15% in the plastic regime (Fig. 4(c)). This difference is actually smaller than the data presented by [19], using different jacketing materials in their experiments. Allowing these errors, lattice strain works as "stress gauge".

Fig. 3 also shows that at lower pressures, lattice strains become more anisotropic with increasing total strain. The magnitude of lattice strain is greatest for 200 and least for 222 in the plastic regime below 2 GPa. At higher pressure (6.4 GPa), the absolute values of lattice strain are still largest for 200 because the first-stage hardening for 200 appears to continue up to 6% total strain. The second-stage hardening parameters are almost the same for 220 and 222, both of which exceed that for 200 at total strains above 5% (Fig. 3). As a result, the three lattice strains converge at 10% total strain. It is expected that the lattice strain for 200 will be below that for 220 and 222 above 10% axial strain. The change in hardening behavior at higher pressure (6.4 GPa) suggests a possible change in flow mechanism. This strain-hardening behavior can also explain the discrepancy in elastic anisotropy observed in previous diffraction experiments and elasticity measurements. Elasticity measurements such as ultrasonics and Brillouin scattering show that elastic anisotropy $S(=S_{11}-S_{12}-S_{44}/2)$ of MgO decreases only modestly with pressure, and predict that S will become zero (isotropic) at a pressure of 11 GPa [17], 19 GPa [20], 21 GPa [21], and 21.5 GPa

[22]. On the other hand, X-ray diffraction studies based on lattice strains concluded that anisotropy diminished at pressures between 2 and 4 GPa in the Drickamer cell [23], around 25 GPa in the DAC [24], or about 8 GPa in the DAC [4]. We attribute the discrepancy to various stress conditions and unknown total strains in previous diffraction studies, owing to the strain-hardening behavior observed in Fig. 3. In previous diffraction experiments, it was assumed that all grains were under identical stress conditions, hence equal lattice strain was interpreted as elastic isotropy (identical $G(hkl)$ in Eq. (3)).

Magnesiowüstite (Mg,Fe)O is believed to coexist with $(Mg,Fe)SiO_3$ perovskite in the Earth's lower mantle, and the rheological property of an end-member MgO are of fundamental importance to infer flow behavior of mantle minerals (e.g., [2,4] and references therein). The strong strain hardening observed in MgO is unlikely to persist under high temperature, because hardening is generally controlled by interactions of dislocations when they are less mobile in the low temperature plastic regime (e.g., [25]). Once the dislocation climb is activated at high temperatures, flow stress is expected to diminish. On the other hand, our results also show that the hardening parameter appears to increase with pressure. Pressure and temperature effects on flow mechanism are therefore of fundamental importance to infer the Earth's mantle dynamics. We have established new experimental technique in conducting high pressure deformation using monochromatic diffraction, and high temperature deformation experiments are underway to quantify the flow models of MgO under simultaneous high pressure and temperature.

5. Uncited reference

[16]

Acknowledgments

We thank A. Hammersley and ESRF personnel for the public use of FIT2D. We also thank T. Duffy, S. Merkel, M. Jessell and reviewers for useful discussion. The synchrotron work was performed at GeoSoilEnviroCARS (GSECARS), Sector 13, Advanced Photon Source at Argonne National Laboratory. We thank N. Lazarz, F. Sopron, M. Jagger, N. Nishiyama and GSECARS personnel for their support during the design and commissioning of the D-DIA. GSECARS is supported by the National Science Foundation—Earth Sciences, Department of Energy—Geosciences, W. M. Keck Foundation, and the U.S. Department of Agriculture. Use of the Advanced Photon Source was supported by the U.S. Department of Energy, Basic Energy Sciences, Office of Energy Research, under Contract No. W-31-109-Eng-38.

References

[1] G.L. Kinsland, W.A. Bassett, Strength of MgO and NaCl polycrystals to confining pressures of 250 kbar at 25 °C, J. Appl. Phys. 48 (1977) 978–984.

[2] C. Meade, R. Jeanloz, Yield strength of MgO to 40 GPa, J. Geophys. Res. 93 (1988) 3261–3269.

[3] D.J. Weidner, Y. Wang, M.T. Vaughan, Yield strength at high pressure and temperature, Geophys. Res. Lett. 21 (1994) 753–756.

[4] S. Merkel, H.R. Wenk, J. Shu, G. Shen, P. Gillet, H.K. Mao, R.J. Hemley, Deformation of polycrystalline MgO at pressures of the lower mantle, J. Geophys. Res. 107 (2002) 2271.

[5] Y. Wang, W.B. Durham, I.C. Getting, D.J. Weidner, The deformation-DIA: a new apparatus for high temperature triaxial deformation to pressures up to 15 GPa, Rev. Sci. Instrum. 74 (2003) 3002–3011.

[6] Y. Wang, M. Rivers, S. Sutton, P. Eng, G. Shen, I. Getting, A multi-anvil, highpressure facility for synchrotron radiation research at GeoSoilEnviroCARS at the Advanced Photon Source, Rev. High Pressure Sci. Technol. 7 (1998) 1490–1495.

[7] M.L. Rivers, T.S. Duffy, Y. Wang, P.J. Eng, S.R. Sutton, G. Shen, A new facility for high-pressure research at the Advanced Photon Source, in: M.H. Manghnani, T. Yagi (Eds.), Properties of Earth and Planetary Materials at High Pressure and Temperature, Geophys. Monogr. Ser., vol. 101, Am. Geophys. Union, Washington, DC, 1998, pp. 79–86.

[8] M.L. Rivers, S.R. Sutton, P. Eng, Geoscience applications of X-ray computed microtomography, in: U. Bonse (Ed.), Developments in X-ray Tomography II, Proceedings of SPIE, vol. 3772, The International Society for Optical Engineering, Washington, 1999, pp. 78–86.

[9] T. Uchida, Y. Wang, M.L. Rivers, S.R. Sutton, Stability field and thermal equation of state of e-iron determined by synchrotron X-ray diffraction in a multianvil apparatus, J. Geophys. Res. 106 (2001) 21799–21810.

[10] A.K. Singh, The lattice strains in a specimen (cubic system) compressed nonhydrostatically in an opposed anvil device, J. Appl. Phys. 73 (1993) 4278–4286.

[11] A.K. Singh, C. Balasingh, The lattice strains in a specimen (hexagonal system) compressed nonhydrostatically in an opposed anvil high pressure setup, J. Appl. Phys. 75 (1994) 4956–4962.
[12] T. Uchida, N. Funamori, T. Yagi, Lattice strains in crystals under uniaxial stress field, J. Appl. Phys. 80 (1996) 739–746.
[13] A.K. Singh, C. Balasingh, H.K. Mao, R.J. Hemley, J. Shu, Analysis of lattice strains measured under nonhydrostatic pressure, J. Appl. Phys. 83 (1998) 7567–7575.
[14] A.P. Hammersley, Fit2d: V9.129 reference manual v3.1, Internal Rep. ESRF98HA01, ESRF, Grendole, France, 1998.
[15] N. Funamori, T. Yagi, T. Uchida, Deviatoric stress measurement under uniaxial compression by a powder X-ray diffraction method, J. Appl. Phys. 75 (1994) 4327–4331.
[16] J.F. Nye, Physical Properties of Crystals, Oxford University Press, 1957.
[17] H. Spetzler, Equation of state of polycrystalline and single-crystal MgO to 8 kilobars and 800 °K, J. Geophys. Res. 75 (1970) 2073–2087.
[18] C.O. Hulse, S.M. Copley, J.A. Pask, Effect of crystal orientation on plastic deformation of magnesium oxide, J. Am. Ceram. Soc. 46 (1963) 317–323.
[19] M.S. Paterson, C.W. Weaver, Deformation of polycrystalline MgO under pressure, J. Am. Ceram. Soc. 53 (1970) 463–471.
[20] G. Chen, R.C. Liebermann, D.J. Weidner, Elasticity of single-crystal MgO to 8 gigapascals and 1600 kelvin, Science 280 (1998) 1913–1916.
[21] I. Jackson, H. Niesler, The elasticity of periclase to 3 GPa and some geophysical implications, in: S. Akimoto, M.H. Manghnani (Eds.), High Pressure Research in Geophysics, CAPJ/Reidel, Tokyo/Dordrecht, 1982, 93–113.
[22] S.V. Sinogeikin, J.D. Bass, Single-crystal elasticity of MgO at high pressure, Phys. Rev. B59 (1999) 14141–14144.
[23] T. Uchida, T. Yagi, K. Oguri, N. Funamori, Analysis of powder X-ray diffraction data obtained under uniaxial stress field, Rev. High Pressure Sci. Technol. 7 (1998) 269–271.
[24] T.S. Duffy, R.J. Hemley, H.K. Mao, Equation of state and shear strength at multimegabar pressures: magnesium oxide to 227 GPa, Phys. Rev. Lett. 74 (1995) 1371–1374.
[25] P. Cordier, Dislocations and slip systems of mantle minerals, in: S. karato, H.R. Wenk (Eds.), Plastic Deformation of Minerals and Rocks, Reviews in Mineralogy & Geochemistry, vol. 51, Mineralogical Society of America, Washington, DC, 2002, pp. 137–179.